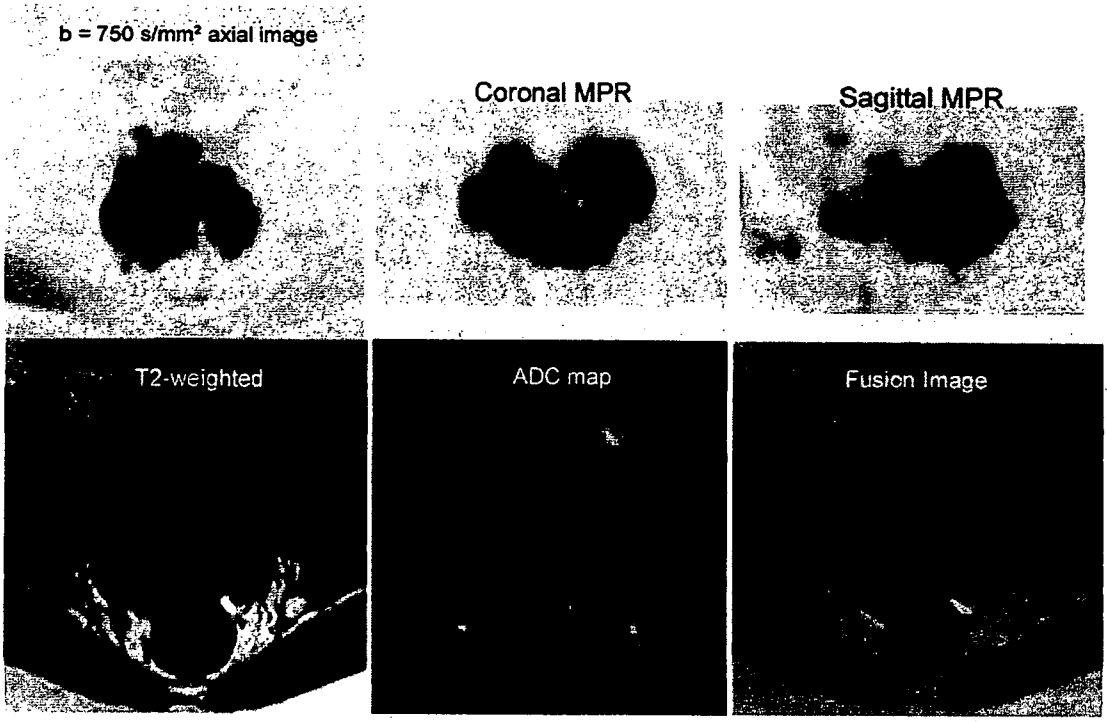

Fig. 1. Free-breathing multiple averaging diffusion-weighted imaging. Study in a 54-year-old woman shows a large mass within the rectouterine pouch that demonstrates restricted diffusion on the b = 750 s/mm² image displayed using an inverted gray scale. Thin image partitions produce images of good signal-to-noise that allow multi-planar reformats. Note the corresponding T_2-weighted image and the apparent diffusion coefficient map. The diffusion-weighted axial image could also be displayed using a color scale (tumor colored red and orange) and fused with the T_2-weighted image to provide combination of functional and anatomical information.

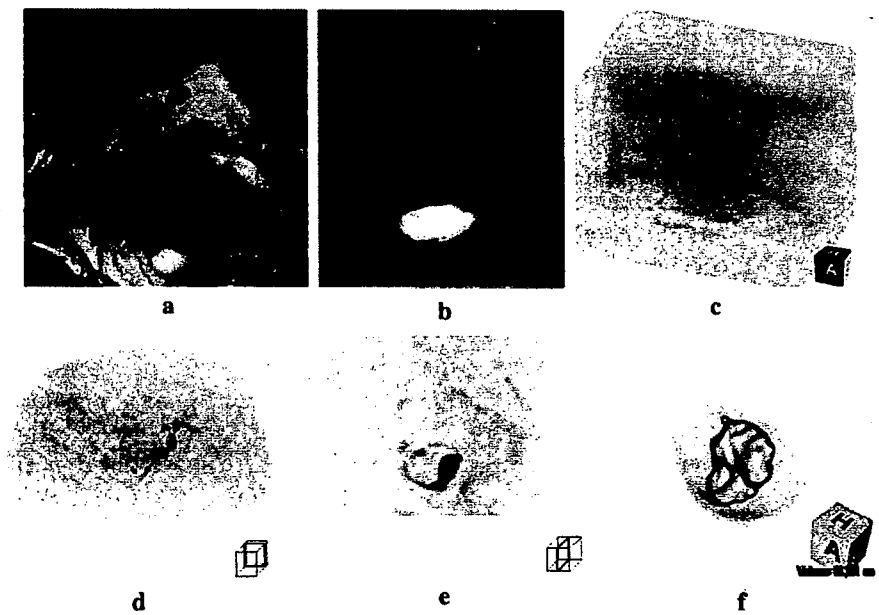

Fig. 2. Three-dimensional displays of diffusion-weighted images with background suppression (DWIBS) technique. A 66-year-old woman with bladder cancer. **(a)** Axial T_2-weighted image shows large bladder cancer in the posterior wall and small daughter nodule anteriorly. **(b)** T_2-weighted magnetic resonance urography shows bilateral hydronephrosis from obstruction of the ureterovesicle junctions. **(c)** Maximum intensity projection of DWIBS image showing main tumor and metastatic left common iliac nodes. **(d)** Axial reformat (8-mm slice thickness, obtained from 4-mm source image) demonstrates metastatic left iliac nodes. **(e)** Sagittal reformat shows main posterior tumor and small anterosuperior daughter nodule. **(f)** Volume rendering image shows 3D shape of the tumor. Images (c) to (f) are derived from one thin section data set.

in imaging selected areas in the body, such as the liver, chemical fat selective saturation (e.g., spectral selected attenuation with inversion recovery [SPAIR], chemical shift selective [CHESS]) or water-selective excitation may be more useful because these methods produce better signal-to-noise because the repetition time is increased using the STIR technique as the nulling period is of the order of 0.693×300 ms per slice. In addition, using conventional STIR imaging, some of the potential signal is lost by the inversion of all spins, including those associated with water molecules. With SPAIR imaging, only the protons associated with fat are affected by the inversion pulse. One practical step to ensure optimum fat suppression is to perform higher order or advance shimming prior to image acquisition.

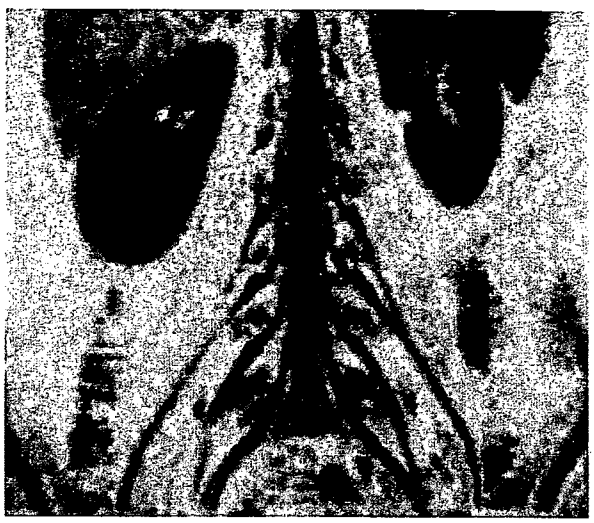

Fig. 3. Diffusion-weighted magnetic resonance neurography. Inverted gray scale maximum intensity projection diffusion-weighted imaging with background suppression image of the lumbar spine of a healthy volunteer showing details of the lumbar plexus.

Minimize T_1 saturation and T_2 shine-through effects. When performing DWI in the body, the repetition time should be sufficiently long to avoid T_1 saturation effects, particularly for the target tissues under evaluation. T_1 saturation can result in spuriously low calculated ADC values. In the liver, for example, malignant lesions such as metastases have a mean T_1 relaxation time of approximately 610 ms.[11] As such, a repetition time of at least 3 times the T_1 relaxation time of the tissue would help to avoid T_1 saturation effects. (N.B. This provides 95% of the longitudinal magnetization recovery. Ideally, a choice of 5 times the T_1 relaxation time of tissue provides 99% magnetization recovery, but this can be impractical, particularly for breath-hold studies). However, even longer repetition times would be required to ensure elimination of this effect in structures with longer T_1 relaxation times (e.g., liver cysts with mean T_1 relaxation time of up to 1 to 2 s).

The other confounding influence on the diffusion-weighted contrast is the T_2 shine-through effect that occurs as a result of high signal intensity

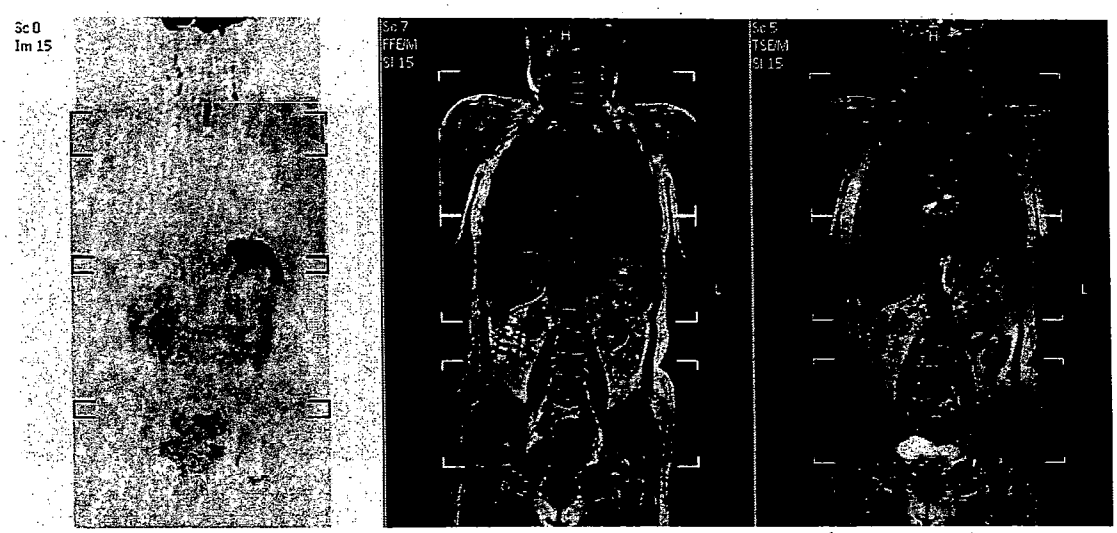

Fig. 4. Example of whole-body diffusion-weighted imaging with background suppression (WB-DWIBS) image obtained from merging 3 image segments acquired using a single coil array. Using the operator console allows merging and display of diffusion- (left), T_1- (middle), and T_2-weighted (right) images from 3 contiguous datasets acquired using the coil sliding technique.

returned from tissues with long intrinsic T_2 relaxation times contributing to the overall measured diffusion-weighted signal. Visual assessment alone may falsely ascribe the high signal intensity observed to restriction in water diffusion. This phenomenon is more difficult to avoid but may be overcome by using an exponential image[12] or calculating the ADC (Fig. 5).

Choice of b-values. When choosing the magnitude and number of b-values to be applied for DWI, considerations should include the DWI technique used, the anticipated image signal-to-noise, the target organ being evaluated, and whether DWI is primarily used for qualitative or quantitative analysis.

When DWI is performed with increasing b-values, the attenuation of the signal intensity in abdominal organs has been shown to be biexponential for the range used for clinical imaging in the body (e.g., b = 0 to 1000 s/mm²). An initial rapid decrease in signal intensity with a small increase in b-value is followed by a more gradual slope of signal attenuation as the b-value increases further. A summary plot derived from published literature values and our own experiments suggests that the initial rapid signal attenuation extends to a b-value of about 100 s/mm² (Fig. 6).

With this in mind, the use of only 2 b-values at DWI[13] will not adequately characterize this biexponential behavior, but it would be possible to derive ADC calculations to reflect this phenomenon using at least 3 b-values. An ADC calculated using only low b-values ($\leq$ 100 s/mm²; sometimes referred to as ADC*fast* or ADC*low*) will be sensitive to intravoxel capillary perfusion. By contrast, ADC calculations derived from images of b-values greater than 100 s/mm² (sometimes referred to as ADC*slow* or ADC*high*) will be relatively perfusion insensitive and theoretically more reflective of tissue cellularity and the integrity of cellular membranes. Of course, ADC can still be calculated over an entire range of b-values, and such an approach has been established in clinical practice for many

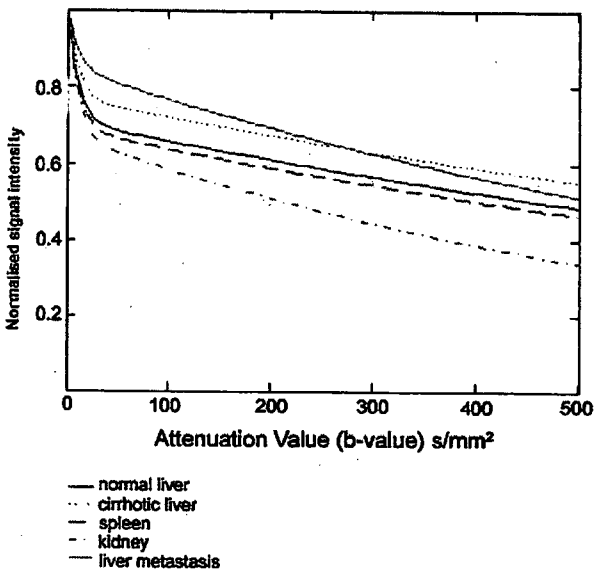

Fig. 6. Signal attenuation in intra-abdominal organs. Graph showing biexponential signal attenuation in major intra-abdominal organs with increasing diffusion weighting. Note the initial rapid signal attenuation with a small increase in b-value, followed by a more gradual slope of signal attenuation beyond approximately b = 100 s/mm².

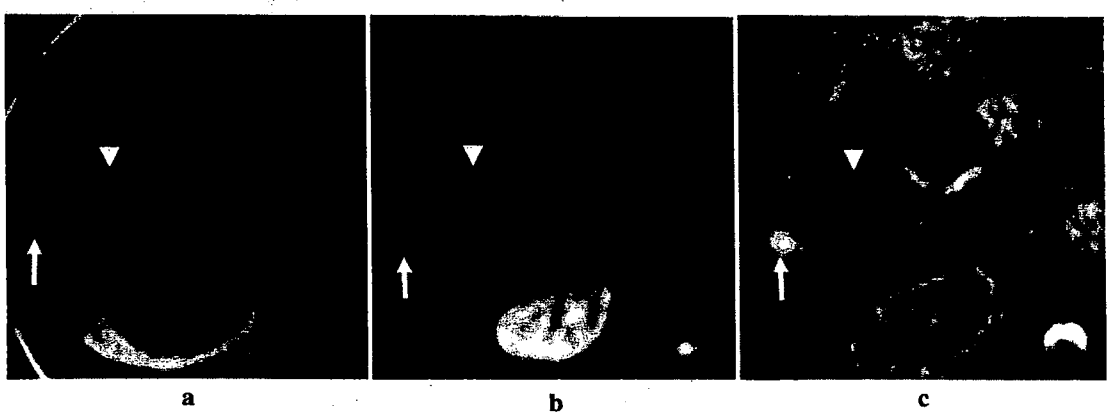

Fig. 5. Overcoming T_2 shine-through using apparent diffusion coefficient (ADC) maps. **(a)** T_1-weighted axial image of the liver showing a small cyst (arrow) and larger metastases (arrowhead). **(b)** At diffusion-weighted imaging, both cyst and metastasis return high signal on b = 500 s/mm² image. **(c)** The ADC map confirms the cyst as showing high ADC (bright) compared with the metastases, which return a low ADC value.

years. Indeed, the intravoxel incoherent motion (IVIM) equation has been applied to characterize the biexponential behavior. However, fractionating the ADC calculations into ADC*fast* and ADC*slow* may potentially be more informative, especially for evaluating treatment response, because drug treatment (e.g., antiangiogenic drug) may reduce blood flow (decrease ADC*fast*) and tissue cellularity (increase ADC*slow*) with little change in overall ADC value. (Fig. 7)

The influence of the choice of b-value on ADC calculations can be observed in the literature. For example, in liver metastases, ADC values calculated using relatively low b-values (e.g., < 100 s/mm^2)[14] are higher than ADC calculations obtained using larger b-values (e.g., > 100 s/mm^2).[13,15-17] It has also been shown that the mean ADC of colorectal liver metastases calculated over a range of b-values (0, 150, and 500 s/mm^2) is higher than that calculated using higher b-values only (150 and 500 s/mm^2).[18] Similarly, ADC*fast* calculated using low b-values are usually higher than ADC*slow* derived from higher b-values (Fig. 8). More recently, it was shown in normal volunteers that portal perfusion exerted a significant effect when a b-value of 200 s/mm^2 was used, and the ADC measurement of the liver was more reproducible when only higher b-values ($b = 500$ and 750 s/mm^2) were employed.[19]

Although it may seem prescriptive to recommend b-values for tumor imaging in the body, DWI for quantifying tumor ADC should include a range of b-values that enables calculation of the ADC*fast* and ADC*slow*. When using non-breath-hold multiple averaging DWI imaging, multiple b-values can be employed to achieve this (e.g., $b = 0$, 50 100, 250, 500, 750 s/mm^2). However, when breath-hold imaging is used, there is a limit to the number of b-values that can be accommodated within each breath-hold without increasing the echo or acquisition time. Thus, the choice of 3 appropriate b-values (e.g., $b = 0$, 100, 500 s/mm^2) is practical when using breath-hold imaging and still enables the fractionating of the ADCs.

Some authors have employed very low b-values (e.g., $b = 3$ s/mm^2) for DWI study.[20] However, ensuring the validity of these small b-values requires proper account of the diffusion weighting introduced by the imaging sequence read-out gradients. Furthermore, some MR systems do not permit the use of very low b-value. Hence, to facilitate meaningful data comparison between centers, it would be useful to ensure that the smallest diffusion weighting applied for imaging can be effectively achieved on other MR systems.

When performing DWIBS, a higher b-value (1000 s/mm^2) is typically used to maximize background signal attenuation and suppression.[7] However, it has to be remembered that the greater signal attenuation at higher b-values usually requires a larger number of signal averages (e.g., $n = 4$ to 6) to maintain good signal and contrast-to-noise.

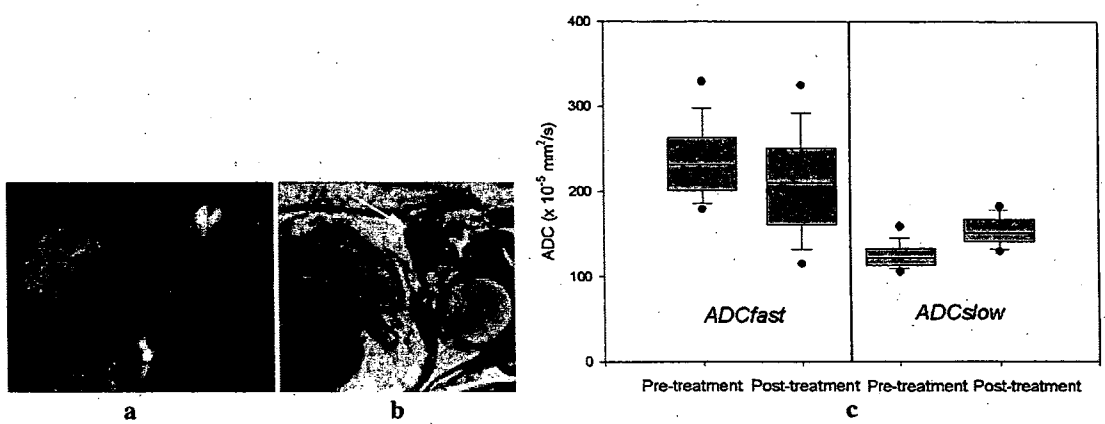

Fig. 7. Evaluating treatment response. Assessment of response made using free-breathing multiple averaging diffusion-weighted imaging, (**a**) apparent diffusion coefficient (ADC)*fast* and (**b**) T_2-weighted image showing an irregular 3-cm left inguinal node (arrow) in a 54-year-old woman with metastatic ovarian cancer. (**c**) Box and Whisker plots of the pixel values of ADC*fast* and ADC*slow* within a region of interest drawn over the lymph node before and at one week after treatment with a novel antivascular drug. Lines through boxes indicate median ADC value, and the whiskers indicate the 5th and 95th percentile values. Rounded circles define the 95% confidence interval. After treatment, there was a significant decrease in the ADC*fast* with a contemporaneous significant increase in the ADC*slow* ($P < 0.001$, Wilcoxon signed rank test).

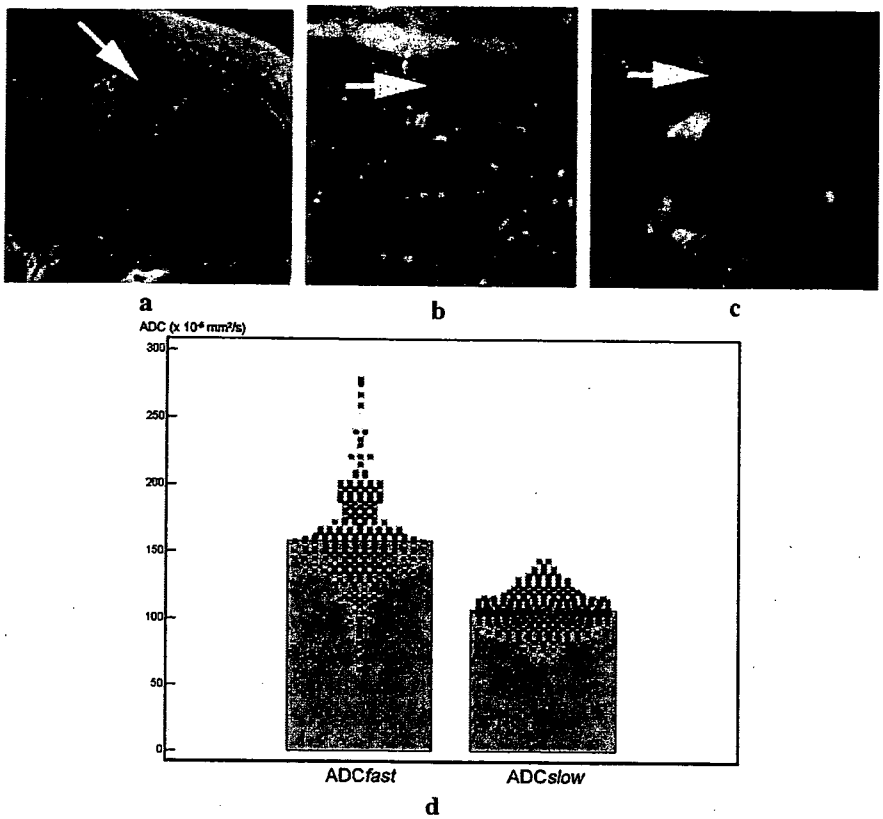

Fig. 8. Apparent diffusion coefficient (ADC)*fast and* ADC*slow*. (**a**) T_2-weighted magnetic resonance imaging showing a 4-cm left external iliac lymph node (arrow). A similar region of interest was drawn encompassing the node (arrows) on the (**b**) ADC*fast* (from b = 0 and 150 s/mm² images) and (**c**) ADC*slow* (from b = 150 and 500 s/mm² images) maps. (**d**) The mean ADC*fast* was higher than the mean ADC*slow* (gray bars). Individual pixel values within the region of interest are plotted as black dots.

Motion-probing gradients. Because water diffusion in tumors and major abdominal organs (except the kidneys) is typically isotropic, it has been suggested that the motion-probing gradient can be applied in just a single direction in abdominal organs showing isotropic diffusion.[13] However, it may still be useful to perform DWI using 3 orthogonal motion-probing gradients in the body to yield both directional and trace DWI images. One clear advantage of calculating the trace image is an improvement in the signal-to-noise ratio by square root of 3 in isotropic regions. In nonisotropic regions (e.g., the kidneys), the trace provides a direction-independent estimate of diffusivity. Review of the directional DWI images can also be helpful when random susceptibility, motion, or EPI artifacts that are present in images of one direction propagate to degrade the trace image.

The use of tetrahedral encoding allows 3 orthogonal motion-probing gradients to be applied simultaneously. Tetrahedral encoding provides the ability to reduce echo-time by combining gradients to obtain high b-values with shorter lengths of MPGs. The reduced echo-time can substantially improve image quality and signal-to-noise and can be used as a strategy to improve the quality of DWI images, but the individual directional images are usually not available for review. Nevertheless, such a technique has been successfully implemented for imaging in the body, including multiple-averaging non-breath-hold DWI.

Reducing artifacts. Diffusion-weighted MR imaging is susceptible to a range of artifacts related to motion, EPI, and susceptibility effects. A detailed account of these is beyond the scope of this article, and the reader is referred to an excellent recent review.[21]

Perhaps, it is worth reflecting upon the nature of motion to which DWI is susceptible. Motion in the body can be thought of as either incoherent or coherent. The former leads to phase dispersion by the motion-probing gradient and results in signal de-

crease at DWI. However, the latter leads only to phase shift and so does not result in significant signal attenuation.

Interestingly, respiratory movement can be viewed as analogous to coherent motion. Muro and colleagues[22] demonstrated this effect in an experiment using fluid-filled phantoms that moved periodically in their long axes along the z-direction of the MR system to simulate respiratory motion. They found that such motion resulted in less than 10% error in ADC measurements of the fluid in the phantom (Fig. 9), and their results suggested that uniform respiratory motion may not lead to significant decrease in DWI signal or substantial errors in ADC measurements, especially over a large nearly uniform structure (e.g., liver). However, respiratory motion can still result in ADC errors in small focal lesions, caused by contamination of signal from adjacent tissues. In addition, movement of the diaphragm at higher speed (or wider excursion) can still lead to blurring of small objects and ADC errors. Bowel peristalsis can also be considered coherent motion (Fig. 10). By contrast, cardiac motion appears to be largely incoherent and can result in severe signal loss in the mediastinum or over the left lobe of the liver (Fig. 11). One technique to minimize such errors and artifacts is to synchronize image acquisition with the source of motion, such as by using cardiac gating and navigator echoes for respiratory triggered acquisitions.

The use of periodically rotated overlapping parallel lines with enhanced reconstruction (PROPELLER) can also help minimize motion effects. PROPELLER is a radial fast spin-echo sequence used with multi-shot imaging. The data is acquired using a series of concentric blades, each of which rotates through the center of the k-space, which reduces any rotation and translation artifacts that occur between the acquisitions of the blades and distributes artifacts uniformly throughout the image.

A major source of artifacts is the eddy currents induced by the rapid switching on and off of the motion-probing gradients, which can lead to geometric distortion as well as image-shearing artifacts that may become more pronounced with increasing

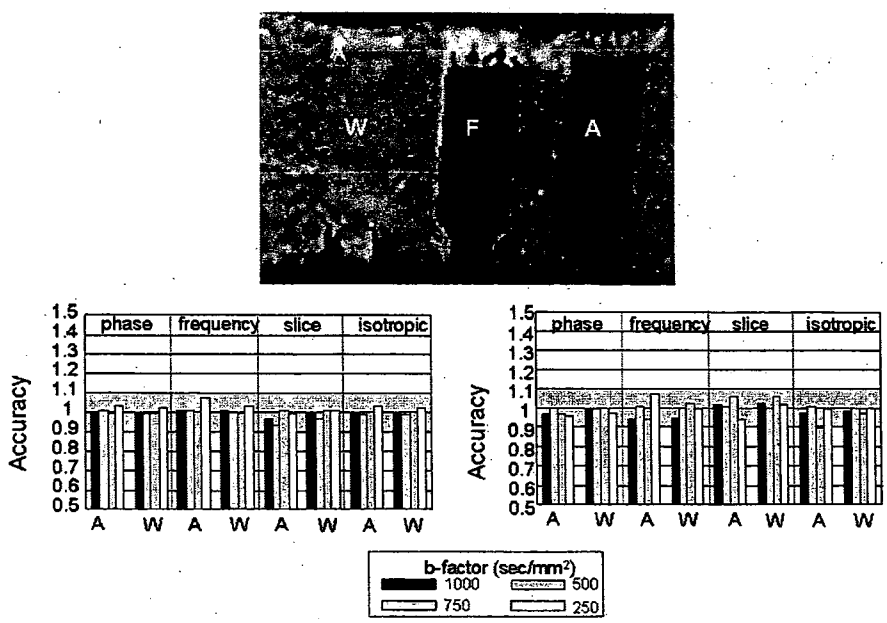

Fig. 9. Effect of motion on apparent diffusion coefficient (ADC) measurements. ADC map of phantoms containing water (W; left), fat (F; middle), and detergent (A; right) embedded in agar. The phantom was scanned moving along the axis of the magnetic resonance scanner simulating respiration. Graphs show the calculated ADC values measured when the phantom was moving at speed of 10 mm/s (lower left) and 20 mm/s (lower right) in the different directions of motion-probing gradients and b-values compared with measurements taken when stationary. Note that the errors for ADC measurement were less than 0.1. This suggests that coherent motion may not affect the ADC measurements. (Permission for reprint obtained by Dr. Takahara from the Nippon Hoshasen Gijutsu Gakkai Zasshi 2005; 61:1551–1558).

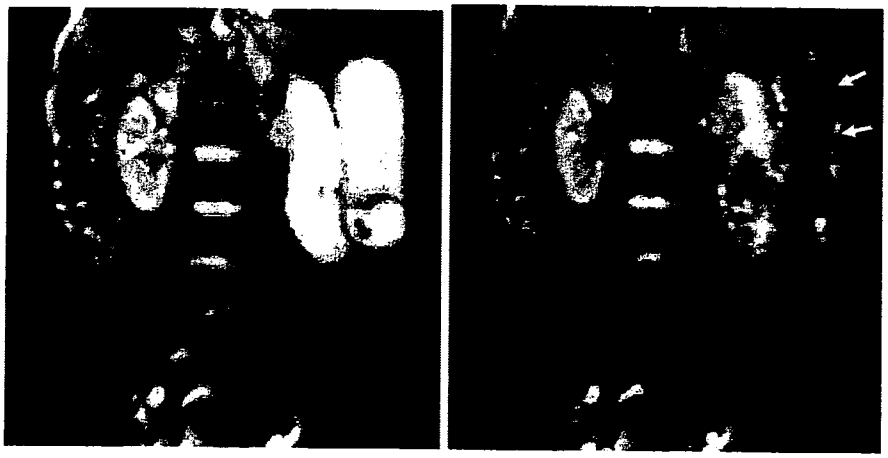

Fig. 10. Small bowel peristalsis. A 52-year-old woman with suspected bowel obstruction. Cine magnetic resonance imaging (not shown) shows good movement in a dilated jejunal loop. Coronal single-shot echo-planar images (**a**) at b = 0 s/mm² and (**b**) at b = 50 s/mm² shows that the signal from the jejunal wall (white arrows) is maintained when diffusion weighting is applied in (**b**). However, there is signal attenuation of the luminal contents. This suggests that peristaltic intestinal wall motion is relatively coherent compared with the incoherent motion of luminal turbulence.

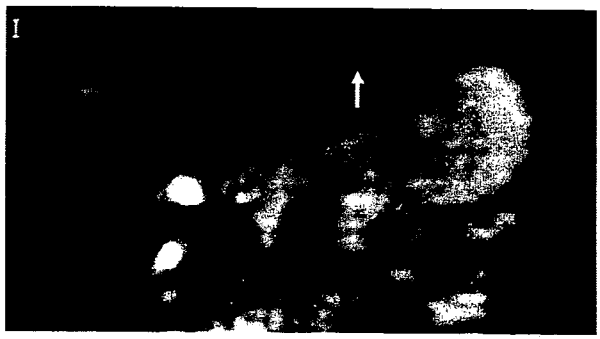

Fig. 11. Signal loss in the left lobe of the liver resulting from cardiac motion. Coronal reformat image of diffusion-weighted imaging (b = 50 s/mm²) shows significant signal attenuation (arrow) over the left lobe of the liver, especially just adjacent to the heart.

b-values. When EPI is employed, there can also be significant magnetization phase shifts that cause "ghosting" artifacts, which are usually worst in the phase-encoding direction. Several adjustments at imaging can help improve image quality, such as changing the band-width, which alters the echo-spacing; and reducing the field of view in the phase encoding direction to a minimum. Increasing the band-width reduces geometric artifacts but can lead to reduction in signal-to-noise and increased ghosting. Because these issues can be complex, it is valuable to engage the expertise of an MR physicist to finely tune the system for optimal performance.

Diffusion-weighted imaging is highly sensitive to susceptibility artifacts. In the abdomen, air in the gastrointestinal tract can cause susceptibility artifacts that obscure visualization of adjacent structures. Intriguingly, it was recently reported that the administration of intravenous Buscopan prior to imaging can worsen the degree of artifacts encountered over the left lobe of the liver.[6]

Quality assurance. To ensure that the MR system is optimized, it is important to develop quality assurance testing as part of the imaging program. One method[23] uses diffusion phantoms made of copper sulphate and sucrose solutions. This allows the precision and accuracy of the ADC measurement to be determined in relation to the noise of the MR imaging system, signal reproducibility, and differences between nominal and effective b-values.[23] In addition, use of these phantoms will allow early recognition of geometric distortion and other eddy current-induced artifacts, thereby enabling their rectification or minimization prior to clinical scanning.

Applications of DWI Techniques for Tumor Assessment

The range of DWI imaging methods described has been employed to assess tumors in the body.[24] Diffusion-weighted imaging has been used to detect[25-28] and characterize[16,29,30] tumors, assess treat-

ment response,[31,32] and provide prognostic information.[33-35] Although not exhaustive, the following account of the clinical applications of DWI illustrates the potential of these techniques.

Breath-hold single shot DWI. Breath-hold single-shot echo planar DWI has been used successfully to evaluate target areas within the abdomen and pelvis. DWI has been applied to detect and characterize tumors in the liver,[18,27,36-40] pancreas,[41] kidneys,[41-45] colon,[46] and prostate.[47,48]

For example, in the liver, breath-hold DWI imaging alone could accurately detect the presence of colorectal hepatic metastases with high sensitivity and specificity[27] (Fig. 12). Application of low diffusion weighting at image acquisition nulls the high signal within intrahepatic blood vessels, thereby facilitating the detection of small metastases lying adjacent to blood vessels. Quantitative ADC measurements can also be calculated using breath-hold DWI, which may aid lesion characterization. It has been shown that malignant hepatic lesions return lower ADC values than do benign lesions, but there is significant overlap.[13] More recently, it was found that high pretreatment ADC values in colorectal hepatic metastases predicted for poor response to chemotherapy.[49] ADC values have also been shown to increase in colorectal hepatic metastases, thus showing at least a partial response to chemotherapy, but not in the nonresponders.[49]

Free-breathing multiple averaging DWI. Free-breathing multiple averaging DWI is a versatile imaging technique that can be applied to virtually any area in the body (Fig. 11). It has been used to evaluate tumors in diverse areas, such as the head and neck,[50,51] pancreas,[25] kidneys,[45,52] and prostate.[53] ADCs can be calculated from the multiple-b-value DWI images acquired, which may help in assessing treatment response.

Diffusion-weighted whole-body imaging with background body signal suppression (DWIBS). Because DWIBS images are usually evaluated qualitatively, the use of just two b-values is usually sufficient ($b = 0$ and $1000\ s/mm^2$). The choice of a higher b-value in combination with fat suppression results in good background suppression. However, more b-values may be accommodated within the measurement to facilitate the calculation of ADCs.

Initial experience in applying the technique to clinical studies has shown substantial promise. However, DWIBS should be interpreted with other imaging sequences because benign lesions may result in false positives, and certain malignant lesions, such as sclerotic bone metastases, can lead to false negative results. Furthermore, because DWIBS discriminates tissues on the basis of cellularity rather than malignancy, its ability to distinguish between benign and malignant lymph nodes remains uncertain. Its implementation in the evaluation of lymphoma appears promising, but further studies evaluating the clinical applications of the technique are being undertaken. There is also considerable interest in establishing the diagnostic accuracy of the technique in tumor detection compared with whole-body STIR imaging and 18-flurodeoxyglucose positron emission tomography.

Conclusions

Diffusion-weighted MR imaging is useful for assessing tumors. In the body, 3 main DWI strategies are currently applied for tumor imaging. These techniques show considerable promise for detecting

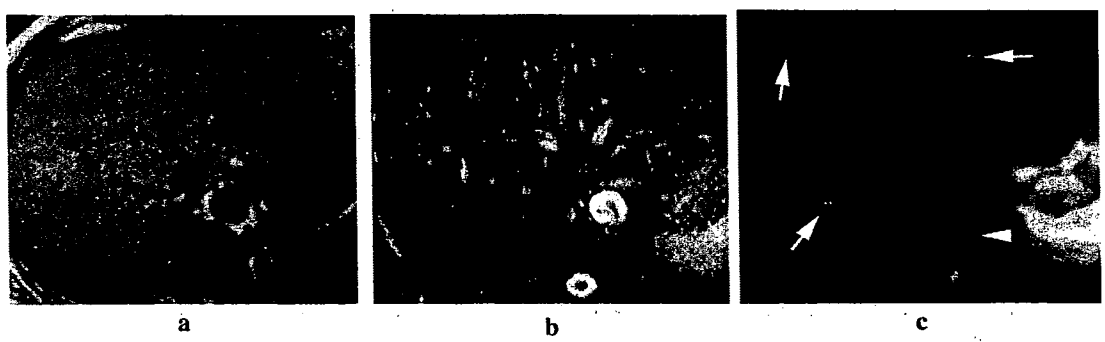

Fig. 12. Lesion detection in the liver using free-breathing diffusion-weighted imaging (DWI). A 45-year-old woman with breast cancer. In this example, metastases were difficult to visualize on the (**a**) unenhanced axial T_1- and (**b**) T_2-weighted images However, at DWI, (**c**) the high signal from intrahepatic vessels is suppressed by application of diffusion gradient on the $b = 100\ s/mm^2$ image, enabling the metastases (arrows) to be clearly identified. Note also the incidental finding of a hemangioma within the vertebral body (arrowhead).

and characterizing tumors and evaluating treatment response. However, careful optimization of these techniques is required to ensure high quality images for both qualitative and quantitative assessment. Radiologists should be acquainted with the key factors that affect the quality of DWI studies to ensure effective implementation of these techniques in clinical practice.

References

1. Bammer R. Basic principles of diffusion-weighted imaging. Eur J Radiol 2003; 45:169–184.
2. Yoshikawa T, Kawamitsu H, Mitchell DG, et al. ADC measurement of abdominal organs and lesions using parallel imaging technique. AJR Am J Roentgenol 2006; 187:1521–1530.
3. Oner AY, Celik H, Oktar SO, Tali T. Single breath-hold diffusion-weighted MRI of the liver with parallel imaging: initial experience. Clin Radiol 2006; 61:959–965.
4. Taouli B, Martin AJ, Qayyum A, et al. Parallel imaging and diffusion tensor imaging for diffusion-weighted MRI of the liver: preliminary experience in healthy volunteers. AJR Am J Roentgenol 2004; 183:677–680.
5. Murtz P, Flacke S, Träber F, van den Brink JS, Gieseke J, Schild HH. Abdomen: diffusion-weighted MR imaging with pulse-triggered single-shot sequences. Radiology 2002; 224:258–264.
6. Nasu K, Kuroki Y, Sekiguchi R, Kazama T, Nakajima H. Measurement of the apparent diffusion coefficient in the liver: is it a reliable index for hepatic disease diagnosis? Radiat Med 2006; 24: 438–444.
7. Takahara T, Imai Y, Yamashita T, Yasuda S, Nasu S, Van Cauteren M. Diffusion weighted whole body imaging with background body signal suppression (DWIBS): technical improvement using free breathing, STIR and high resolution 3D display. Radiat Med 2004; 22:275–282.
8. Nasu K, Kuroki Y, Sekiguchi R, Nawano S. The effect of simultaneous use of respiratory triggering in diffusion-weighted imaging of the liver. Magn Reson Med Sci 2006; 5:129–136.
9. Spuentrup E, Buecker A, Koelker C, Guenther RW, Stuber M. Respiratory motion artifact suppression in diffusion-weighted MR imaging of the spine. Eur Radiol 2003; 13:330–336.
10. Takahara T, Yamashita T, Yanagimachi N, Iino M, Koizumi J, Imai Y. Imaging of peripheral nerve disease using diffusion-weighted neurography (DWN) [Abstract SSE13-03], In: Radiological Society of North America Scientific Assembly and Annual Meeting. Chicago, 2004; 394.
11. Farraher SW, Jara H, Chang KJ, Ozonoff A, Soto JA. Differentiation of hepatocellular carcinoma and hepatic metastasis from cysts and hemangiomas with calculated T_2 relaxation times and the T_1/T_2 relaxation times ratio. J Magn Reson Imaging 2006; 24:1333–1341.
12. Provenzale JM, Engelter ST, Petrella JR, Smith JS, MacFall JR. Use of MR exponential diffusion-weighted images to eradicate T_2 "shine-through" effect. AJR Am J Roentgenol 1999; 172:537–539.
13. Taouli B, Vilgrain V, Dumont E, Daire JL, Fan B, Menu Y. Evaluation of liver diffusion isotropy and characterization of focal hepatic lesions with two single-shot echo-planar MR imaging sequences: prospective study in 66 patients. Radiology 2003; 226:71–78.
14. Ichikawa T, Haradome H, Hachiya J, Nitatori T, Araki T. Diffusion-weighted MR imaging with a single-shot echoplanar sequence: detection and characterization of focal hepatic lesions. AJR Am J Roentgenol 1998; 170:397–402.
15. Müller MF, Prasad PV, Siewert B, Edelman RR. [The *in-vivo* diffusion measurements of the liver, kidneys, spleen and m. erector with an echo-planar imaging system in normal subjects]. Rofo 1994; 161:233–236. (Article in German)
16. Namimoto T, Yamashita Y, Sumi S, Tang Y, Takahashi M. Focal liver masses: characterization with diffusion-weighted echo-planar MR imaging. Radiology 1997; 204:739–744.
17. Yamada I, Aung W, Himeno Y, Nakagawa T, Shibuya H. Diffusion coefficients in abdominal organs and hepatic lesions: evaluation with intravoxel incoherent motion echo-planar MR imaging. Radiology 1999; 210:617–623.
18. Koh DM, Scurr E, Collins DJ, et al. Colorectal hepatic metastases: quantitative measurements using single-shot echo-planar diffusion-weighted MR imaging. Eur Radiol 2006; 16:1898–1905.
19. Hollingsworth KG, Lomas DJ. Influence of perfusion on hepatic MR diffusion measurement. NMR Biomed 2006; 19:231–235.
20. Moteki T, Horikoshi H. Evaluation of hepatic lesions and hepatic parenchyma using diffusion-weighted echo-planar MR with three values of gradient b-factor. J Magn Reson Imaging 2006; 24:637–645.
21. Le Bihan D, Poupon C, Amadon A, Lethimonnier F. Artifacts and pitfalls in diffusion MRI. J Magn Reson Imaging 2006; 24:478–488.
22. Muro I, Takahara T, Horie T, et al. [Influence of respiratory motion in body diffusion weighted imaging under free breathing (examination of a moving phantom)]. Nippon Hoshasen Gijutsu Gakkai Zasshi 2005; 61:1551–1558. (Article in Japanese)
23. Delakis I, Moore EM, Leach MO, De Wilde JP. Developing a quality control protocol for diffusion imaging on a clinical MRI system. Phys Med Biol 2004; 49:1409–1422.
24. Koh DM, Collins DJ. Diffusion-weighted MRI in the body: applications and challenges in oncology.

AJR Am J Roentgenol 2007; 188:1622–1635.
25. Ichikawa T, Erturk SM, Motosugi U, et al. High-b value diffusion-weighted MRI for detecting pancreatic adenocarcinoma: preliminary results. AJR Am J Roentgenol 2007; 188:409–414.
26. Ichikawa T, Erturk SM, Motosugi U, et al. High-B-value diffusion-weighted MRI in colorectal cancer. AJR Am J Roentgenol 2006; 187:181–184.
27. Nasu K, Kuroki Y, Nawano S, et al. Hepatic metastases: diffusion-weighted sensitivity-encoding versus SPIO-enhanced MR imaging. Radiology 2006; 239:122–130.
28. Naganawa S, Sato C, Nakamura T, et al. Diffusion-weighted images of the liver: comparison of tumor detection before and after contrast enhancement with superparamagnetic iron oxide. J Magn Reson Imaging 2005; 21:836–840.
29. Chan JH, Tsui EY, Luk SH, et al. Diffusion-weighted MR imaging of the liver: distinguishing hepatic abscess from cystic or necrotic tumor. Abdom Imaging 2001; 26:161–165.
30. Kim T, Murakami T, Takahashi S, Hori M, Tsuda K, Nakamura H. Diffusion-weighted single-shot echoplanar MR imaging for liver disease. AJR Am J Roentgenol 1999; 173:393–398.
31. Byun WM, Shin SO, Chang Y, Lee SJ, Finsterbusch J, Frahm J. Diffusion-weighted MR imaging of metastatic disease of the spine: assessment of response to therapy. AJNR Am J Neuroradiol 2002; 23:906–912.
32. Chen CY, Li CW, Kuo YT, et al. Early response of hepatocellular carcinoma to transcatheter arterial chemoembolization: choline levels and MR diffusion constants–initial experience. Radiology 2006; 239:448–456.
33. Mardor Y, Roth Y, Ochershvilli A, et al. Pretreatment prediction of brain tumors' response to radiation therapy using high b-value diffusion-weighted MRI. Neoplasia 2004; 6:136–142.
34. Dzik-Jurasz A, Domenig C, George M, et al. Diffusion MRI for prediction of response of rectal cancer to chemoradiation. Lancet 2002; 360:307–308.
35. Provenzale JM, Mukundan S, Barboriak DP. Diffusion-weighted and perfusion MR imaging for brain tumor characterization and assessment of treatment response. Radiology 2006; 239:632–649.
36. Okada Y, Ohtomo K, Kiryu S, Sasaki Y. Breath-hold T_2-weighted MRI of hepatic tumors: value of echo planar imaging with diffusion-sensitizing gradient. J Comput Assist Tomogr 1998; 22:364–371.
37. Abe Y, Yamashita Y, Tang Y, Namimoto T, Takahashi M. Calculation of T_2 relaxation time from ultrafast single shot sequences for differentiation of liver tumors: comparison of echo-planar, HASTE, and spin-echo sequences. Radiat Med 2000; 18:7–14.
38. Yamashita Y, Tang Y, Takahashi M. Ultrafast MR imaging of the abdomen: echo planar imaging and diffusion-weighted imaging. J Magn Reson Imaging 1998; 8:367–374.
39. Ito K, Mitchell DG, Matsunaga N. MR imaging of the liver: techniques and clinical applications. Eur J Radiol 1999; 32:2–14.
40. Quan XY, Sun XJ, Yu ZJ, Tang M. Evaluation of diffusion weighted imaging of magnetic resonance imaging in small focal hepatic lesions: a quantitative study in 56 cases. Hepatobiliary Pancreat Dis Int 2005; 4:406–409.
41. Chow LC, Bammer R, Moseley ME, Sommer FG. Single breath-hold diffusion-weighted imaging of the abdomen. J Magn Reson Imaging 2003; 18: 377–382.
42. Squillaci E, Manenti G, Di Stefano F, Miano R, Strigari L, Simonetti G. Diffusion-weighted MR imaging in the evaluation of renal tumours. J Exp Clin Cancer Res 2004; 23:39–45.
43. Squillaci E, Manenti G, Cova M, et al. Correlation of diffusion-weighted MR imaging with cellularity of renal tumours. Anticancer Res 2004; 24:4175–4179.
44. Cova M, Squillaci E, Stacul F, et al. Diffusion-weighted MRI in the evaluation of renal lesions: preliminary results. Br J Radiol 2004; 77:851–857.
45. Pozzi-Mucelli R. Can diffusion-weighted MRI without breath-holding be used to evaluate renal abnormalities? Nat Clin Pract Nephrol 2006; 2:126–127.
46. Nasu K, Kuroki Y, Kuroki S, Murakami K, Nawano S, Moriyama N. Diffusion-weighted single shot echo planar imaging of colorectal cancer using a sensitivity-encoding technique. Jpn J Clin Oncol 2004; 34:620–626.
47. Hosseinzadeh K, Schwarz SD. Endorectal diffusion-weighted imaging in prostate cancer to differentiate malignant and benign peripheral zone tissue. J Magn Reson Imaging 2004; 20:654–661.
48. Reinsberg SA, Payne GS, Riches SF, et al. Combined use of diffusion-weighted MRI and ^{1}H MR spectroscopy to increase accuracy in prostate cancer detection. AJR Am J Roentgenol 2007; 188:91–98.
49. Koh DM, Scurr E, Collins DJ, et al. Predicting response of colorectal hepatic metastases: value of pre-treatment apparent diffusion coefficients. AJR Am J Roentgenol 2007; 188:1001–1008
50. Koç O, Paksoy Y, Erayman I, Kivrak AS, Arbag H. Role of diffusion weighted MR in the discrimination diagnosis of the cystic and/or necrotic head and neck lesions. Eur J Radiol 2007; 62:205–213.
51. Vandecaveye V, De Keyzer F, Nuyts S, et al. Detection of head and neck squamous cell carcinoma with diffusion weighted mri after (chemo) radiotherapy: Correlation between radiologic and histopathologic findings. Int J Radiat Oncol Biol Phys 2007; 67:960–971.
52. Thoeny HC, De Keyzer F, Oyen RH, Peeters RR.

Diffusion-weighted MR imaging of kidneys in healthy volunteers and patients with parenchymal diseases: initial experience. Radiology 2005; 235: 911–917.

53. Kurhanewicz J, Vigneron DB, Males RG, Swanson MG, Yu KK, Hricak H. The prostate: MR imaging and spectroscopy. Present and future. Radiol Clin North Am 2000; 38:115–138, viii-ix.

ELSEVIER

European Journal of Radiology 64 (2007) 375–380

EJR

www.elsevier.com/locate/ejrad

Influences of prolonged apnea and oxygen inhalation on pulmonary hemodynamics during breath holding: Quantitative assessment by velocity-encoded MR imaging with SENSE technique

Munenobu Nogami [a,*], Yoshiharu Ohno [a], Takanori Higashino [a,b], Daisuke Takenaka [a], Takeshi Yoshikawa [a,c], Hisanobu Koyama [a], Hideaki Kawamitsu [d], Masahiko Fujii [a,d], Kazuro Sugimura [a]

[a] *Department of Radiology, Kobe University Graduate School of Medicine, 7-5-2 Kusunoki-cho, Chuo-ku, Kobe, Hyogo 650-0017, Japan*
[b] *Department of Radiology, Tenri Hospital, Tenri, Nara, Japan*
[c] *Department of Radiology, Konan Hospital, Kobe, Hyogo, Japan*
[d] *Division of Radiology, Kobe University Hospital, Kobe, Hyogo, Japan*

Received 31 January 2007; received in revised form 2 February 2007; accepted 2 February 2007

Abstract

Purpose: The purpose of our study was to assess the influence of prolonged apnea and administration of oxygen on pulmonary hemodynamics during breath holding (BH) by using velocity-encoded MR imaging combined with the SENSE technique (velocity MRI).
Materials and methods: Ten healthy male volunteers underwent velocity MRI during BH with and without O_2 inhalation. All velocity MRI data sets were obtained continuously with the 2D cine phase-contrast method during a single BH period. The data were then divided into three BH time phases as follows: first, second and third. To evaluate the influence of prolonged apnea on hemodynamics, stroke volume (SV) and maximal change in flow rate during ejection (MCFR) of second and third phases were statistically compared with those of first phase by using the ANOVA followed by Turkey's HSD multiple comparison test. To assess the influence of O_2 on hemodynamics, SV and MCFR with or without O_2 were compared by the paired *t*-test. To assess the measuring agreement of hemodynamic indices during prolonged breath holding, Bland–Altman's analysis was performed.
Results: Prolonged apnea had no significant influence on SV and MCFR regardless of administration of O_2 ($p > 0.05$). Mean MCFR for all phases was significantly lower with administration of O_2 than without ($p < 0.05$). The limits of agreement for MCFR with O_2 were smaller than without.
Conclusion: O_2 inhalation modulated maximal change in flow rate during ejection, and did not influence stroke volume during breath holding. Influence of O_2 inhalation should be considered for MR measurements of pulmonary hemodynamics during breath holding.

Keywords: Lung; MR imaging; Oxygen; Perfusion; Blood flow; Vascular resistance

1. Introduction

Quantitative assessment of regional pulmonary perfusion using dynamic contrast-enhanced MR imaging has been dramatically improved due to recent advances in MR systems, utilization of contrast media and application of software for quantitative analysis, similar to the advances in nuclear medicine and brain perfusion MR studies [1,2]. For this approach, the indicator dilution theory and the central volume principle, which have been adopted for the construction of time–concentration curves of the main pulmonary trunk in terms of arterial input function, are commonly applied [1,3]. For these regional pulmonary perfusion studies, a breath-holding protocol has been widely used to reduce artifacts derived from respiratory motion. Breath holding is voluntary behavior and overrides automatic ventilation control. Therefore, prolonged apnea due to long breath holding can induce poor gas exchange and influence physiological parameters [4–6]. When the arterial blood volume or flow of the main pulmonary trunk is utilized as the arterial input function, in a manner similar to the previously reported quantitative assessment of dynamic contrast-enhanced MR perfusion imaging, the influence of prolonged apnea may result in unsat-

* Corresponding author at: Tel.: +81 78 382 6104; fax: +81 78 382 6129.
E-mail address: aznogami@med.kobe-u.ac.jp (M. Nogami).

0720-048X/$ – see front matter © 2007 Elsevier Ireland Ltd. All rights reserved.
doi:10.1016/j.ejrad.2007.02.043

isfactory measurements of regional perfusion parameters in the lung [1]. Inhalation of 100% oxygen (O_2) before breath holding is sometimes used for protocols which require longer acquisition time, so that subjects can hold their breath longer and more easily. Although variations in stroke volume resulting from different breath holding protocols (i.e., inspiratory and expiratory breath holding) and the changes in left ventricular stroke volume during normal breathing and Valsalva maneuver have been described in the literature [4,7–9], the influence of inhalation of O_2 on hemodynamic indices during breath holding has, as far as we know, not yet been addressed.

Two-dimensional (2D) or three-dimensional (3D) phase-contrast (PC) MR imaging is currently in use as a velocity-encoded MR imaging (velocity MRI) modality for assessment of hemodynamics of pulmonary or cardiac circulation [10–12]. This technique is suitable for repeated measurements under different conditions without the need for the administration of contrast media. In addition, parallel imaging techniques such as sensitivity encoding (SENSE) yields a short scan time and reproducible measurement of hemodynamic indices during a single breath-holding period [13–15]. This technique has therefore the potential capability of detecting the changes in pulmonary hemodynamics and the influence of O_2 during breath holding.

We hypothesized that prolonged apnea and the inhalation of "100%" oxygen before the breath-holding time may affect the measurements of pulmonary hemodynamics performed by this technique. The purpose of our study was thus to assess the influence of prolonged apnea and administration of oxygen on pulmonary hemodynamics during breath holding by using velocity-encoded MR imaging combined with the SENSE technique.

2. Materials and methods

2.1. Subjects

Ten healthy male volunteers (32.6 years; range, 30–38 years) without any history of cardiovascular or lung events underwent velocity MRI. The ethics committee of our institute approved this study, and written informed consent was obtained from all the volunteers before their enrollment in the study.

2.2. Velocity-encoded MRI techniques

All velocity MRI were performed with a 1.5 T MR scanner (Gyroscan Intera T-15; Philips Medical Systems, Best, the Netherlands) using a four-channel cardiac phased array surface coil. For data acquisition of velocity MRI for the perpendicular section to the assessed vessel for each of the subjects, sagittal and oblique coronal images, positioned parallel to the direction of the main pulmonary artery, were obtained [16] by using a 2D balanced-fast field echo (FFE) sequence (TR 3.3–3.7 ms/TE 1.7–1.9 ms/flip angle 60°, 256 × 256 matrix, 320 mm field of view, 5 mm section thickness) during expiratory breath holding.

For flow measurements, all velocity MRIs were planned in a double oblique section perpendicular to the main pulmonary artery and 2 cm above the pulmonary valve determined from balanced-FFE images [16]. The velocity MRIs were performed with a cine 2D PC sequence (TR 5.3 ms/TE 3.0 ms/flip angle 15°, 256 × 256 matrix, 350 mm field of view, 10 mm section thickness) using retrospective electrocardiogram (ECG)-triggering and SENSE. The velocity encoding gradient was adjusted to 150 cm/s without aliasing, and the reduction factor for SENSE was three. Twenty time frames for one cardiac cycle were obtained (mean 14 s, ranged 10–22 s), yielding a temporal resolution of 35–55 ms, depending on the subject's heart rate.

To assess the hemodynamics of pulmonary circulation during prolonged breath holding, velocity MRI was repeatedly scanned without preparation interval during a single expiratory breath hold and was reconstructed after the acquisition (Fig. 1). Repetition of scanning during a single breath hold was continued three or four times (average 42 or 56 s, respectively) depending on the subject's breath holding ability. Thus, velocity MRI data sets of three or four cardiac cycles during a single breath hold could be acquired.

To evaluate the effect of inhalation of oxygen on pulmonary hemodynamics, velocity MRI data were acquired during inhalation of room air, followed by inhalation of 100% oxygen (3 l/min). The starting point of velocity MRI data acquisition during administration of O_2 was at least 5 min after the subject started O_2 inhalation. Oxygen was continuously supplied throughout the scanning period by means of a non-rebreathing ventilation mask with reservoir bag.

2.3. Monitoring of physiologic parameter

In each subject, heart rate (HR) and oxygen saturation (SpO_2) were monitored as physiological parameters and recorded throughout the study by using a commercially available pulse oxymeter for MRI (8600FO; Nonin Medical, Inc., North Plymouth, MN, USA). The temporal resolution of the pulse oxymeter was 2 s.

2.4. Image analysis of velocity encoded MRI

All velocity MRI data were analyzed on the MRI scanner by using the manufacturer's software (Philips Medical Systems, Best, The Netherlands). All regions of interests (ROIs) outlining the vessel wall of the pulmonary trunk and with a cross-sectional area ranging from 3.0 to 11.3 cm^2, were drawn manually on magnitude images (Fig. 2). Each ROI was then copied onto the phase image from the corresponding magnitude image. Area and mean velocity in the ROI on the phase image were automatically calculated throughout one cardiac cycle, after which the time–velocity curve of the cardiac cycle (*R–R* interval) in the ROI were reconstructed automatically.

Using the time–velocity curve of each velocity MRI data set, each of the hemodynamic indices of stroke volume (SV) and maximal change in flow rate during ejection (MCFR) was assessed. SV was obtained by integration of the time–velocity curve during systole, and MCFR was defined as the maximal value of the ascending slope of the time–velocity curve

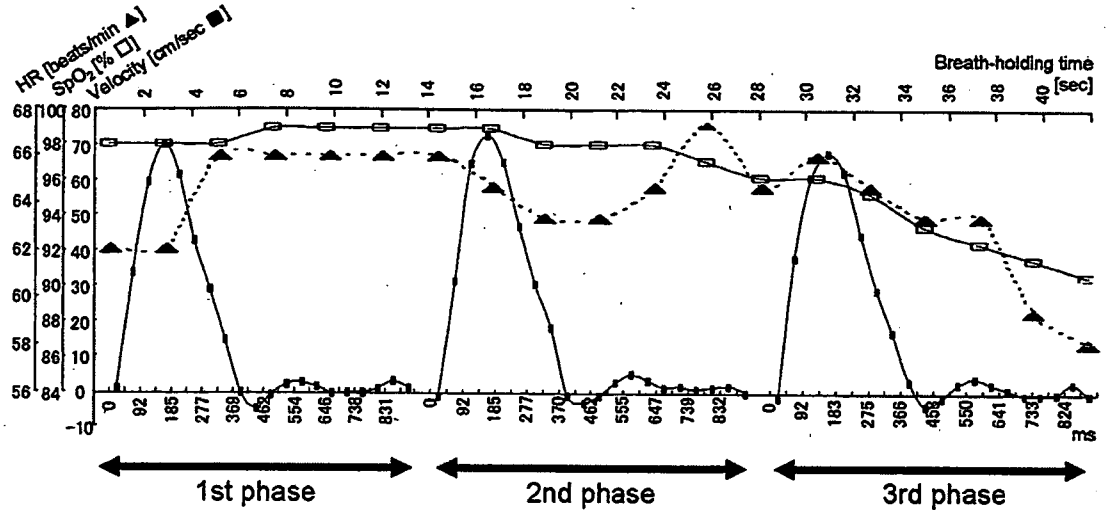

Fig. 1. Example of time–velocity curves acquired during single breath hold. Three data sets (first, second and third phase) of velocity MRI were acquired continuously without preparation intervals during a single breath hold.

during systole (Fig. 2). MCFR is reportedly correlated with pulmonary vascular resistance and is described in the past literature [10]. Hemodynamic indices were calculated from the previously described ROI data with commercially available software (Microsoft Office Excel; Microsoft, Redmond, WA, USA).

2.5. Statistical analysis

For assessment of physiological parameters and pulmonary hemodynamics during breath holding, breath-holding periods were divided into three phases: first, second and third phases. The velocity MRI data sets of a cardiac cycle acquired first, second and third during breath holding were referred as the hemodynamic parameters of the first, second and third phase for all subjects, respectively. For each subject with four data sets ($n=4$), the fourth velocity MRI data set of a cardiac cycle acquired during breath holding was not assessed. Values for HR and SpO_2 were also averaged for each phase.

To evaluate the influence of prolonged apnea on physiological parameters and hemodynamic indices during the breath-holding period, HR, SpO_2, SV and MCFR of second and third phase were statistically compared with those of first phase by using the analysis of variance (ANOVA) followed by Turkey's Honestly Significant Difference (HSD) multiple comparison test.

To assess the influence of O_2 on physiological parameters and pulmonary hemodynamics during breath holding, HR, SpO_2, SV and MCFR were statistically compared between without and with administration of O_2 for each phase by using the paired t-test.

To assess the measuring agreement of hemodynamic indices during prolonged breath holding without and with administration of O_2, the limits of agreement of SV and MCFR between the first and second phase and those between the first and third phase were assessed by means of Bland and Altman's analysis [17]. 95% confidence interval (CI) for the bias and the 95% CIs of lower and upper limits of agreement were also calculated.

p values of less than 0.05 were considered statistically significant.

3. Results

Breath holding time for first phase, first and second phase and first through third phase were 14, 28 and 42 s, respectively.

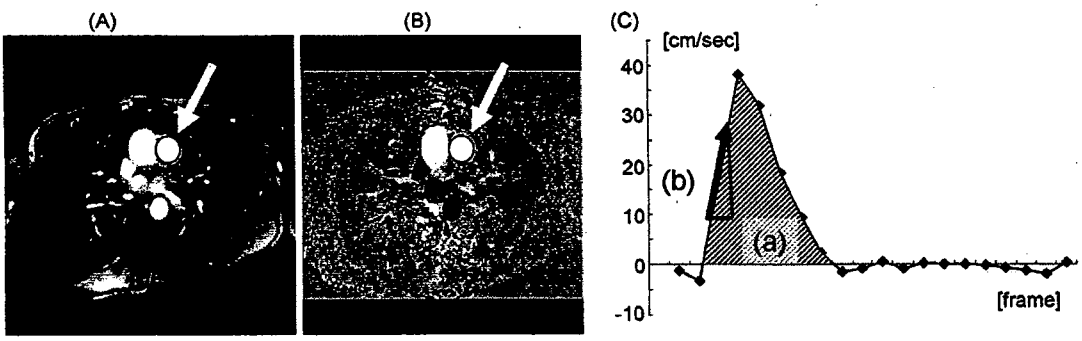

Fig. 2. Example of ROI on magnitude and phase images and time–velocity curve in the ROI. (A) Region of interest (ROI) outlining the pulmonary trunk is drawn manually on magnitude image. (B) Same ROI is copied onto the corresponding phase image. (C) Time–velocity curve in the ROI during a cardiac cycle was automatically reconstructed, and hemodynamic indices including stroke volume (a, SV) and maximal change in flow rate during ejection (b, MCFR) were assessed.

Table 1
Results of comparisons of heart rate (HR), oxygen saturation (SpO_2), stroke volume (SV) and maximal change in flow rate during ejection (MCFR) during breath holding with and without administration of O_2

	First phase (mean ± S.D.)	Second phase (mean ± S.D.)	Third phase (mean ± S.D.)
HR (beats/min)			
Without O_2	71.9 ± 8.9	71.5 ± 7.0	72.6 ± 7.7
With O_2	71.1 ± 8.9	70.2 ± 8.1	69.2 ± 6.2[a]
SpO_2 (%)			
Without O_2	97.9 ± 0.7	97.2 ± 1.5	95.4 ± 2.9[b]
With O_2	98.9 ± 0.6[a]	98.9 ± 0.6[a]	98.4 ± 0.9[a]
SV (ml)			
Without O_2	77.8 ± 8.4	76.9 ± 7.8	74.6 ± 6.9
With O_2	75.4 ± 6.7	74.3 ± 7.3	71.7 ± 7.2
MCFR			
Without O_2	0.61 ± 0.13	0.74 ± 0.19	0.63 ± 0.25
With O_2	0.35 ± 0.08[a]	0.33 ± 0.07[a]	0.30 ± 0.09[a]

S.D.: standard deviation.
[a] Significant difference between without and with O_2 ($p < 0.05$).
[b] Significant difference with the value for first phase ($p < 0.05$).

Mean and standard deviations of HR, SpO_2, SV and MCFR for each phase during breath holding are shown in Table 1. There was no significant difference in HR, SV and MCFR between first and second and between first and third phases ($p > 0.05$). Mean HR for third phase with administration of O_2 was significantly lower than without ($p < 0.05$). Mean SpO_2 without administration of O_2 for third phase was significantly lower than first phase. Mean SpO_2 for all phases was significantly higher with adminis-

Table 2
Mean differences and limits of agreement of SV and MCFR between first and second phases and between first and third phases with either breath holding method by administration of O_2

	Between first and second phases	Between first and third phases
SV (ml)		
Without O_2		
Mean difference (ml)	0.9	3.2
(95% CI of mean difference) (ml)	(−1.2 to 3.0)	(0.1–6.3)
Upper limits of agreement (ml)	6.7	11.9
(95% CI of upper limits of agreement) (ml)	(3.1–10.2)	(6.5–17.3)
Lower limits of agreement (ml)	−4.9	−5.5
(95% CI of lower limits of agreement) (ml)	(−8.4 to −1.3)	(−10.9 to −0.1)
With O_2		
Mean difference (ml)	1.2	3.7
(95% CI of mean difference) (ml)	(−0.7 to 3.0)	(0.8 to 6.6)
Upper limits of agreement (ml)	6.3	11.9
(95% CI of upper limits of agreement) (ml)	(3.1–9.5)	(6.8–17.0)
Lower limits of agreement (ml)	−4.0	−4.5
(95% CI of lower limits of agreement) (ml)	(−7.2 to −0.8)	(−9.6 to 0.6)
MCFR		
Without O_2		
Mean difference	−0.13	−0.02
(95% CI of mean difference)	(−0.28 to 0.01)	(−0.15 to 0.10)
Upper limits of agreement	0.27	0.31
(95% CI of upper limits of agreement)	(0.02–0.51)	(0.10–0.52)
Lower limits of agreement	−0.53	−0.36
(95% CI of lower limits of agreement)	(−0.78 to −0.28)	(−0.57 to −0.15)
With O_2		
Mean difference	0.02	0.05
(95% CI of mean difference)	(−0.01 to 0.05)	(−0.01 to 0.12)
Upper limits of agreement	0.10	0.23
(95% CI of upper limits of agreement)	(0.05–0.16)	(0.12–0.35)
Lower limits of agreement	−0.07	−0.13
(95% CI of lower limits of agreement)	(−0.12 to −0.01)	(−0.24 to −0.02)

CI: confidence interval.

tration of O_2 than without ($p < 0.05$). Mean MCFR for all phases was significantly lower with administration of O_2 than without ($p < 0.05$).

Results of Bland and Altman's analyses of SV and MCFR between first and second phases and between first and third phases are shown in Table 2. Mean differences for SV between the first and second phase without and with administration of O_2 were 0.9 and 1.2 ml, respectively. The limits of agreement for SV without administration of O_2 were between −4.9 and 6.7 ml (i.e. 0.9 ± 5.8 ml), and between −4.0 ml and 6.3 ml (i.e. 1.2 ± 5.1 ml) with O_2 administration. Mean differences between the first and third phase without and with administration of O_2 were 3.2 and 3.7 ml, respectively. The limits of agreement for SV without O_2 administration were between −5.5 and 11.9 ml (i.e. 3.2 ± 8.7 ml), and between −4.5 and 11.9 ml (i.e. 3.7 ± 8.2 ml) with O_2 administration.

Mean differences for MCFR between the first and second phase without and with administration of O_2 were −0.13 and 0.02, respectively. The limits of agreement for MCFR without administration of O_2 were between −0.53 and 0.27 (i.e. -0.13 ± 0.40), and between −0.07 and 0.10 (i.e. 0.02 ± 0.09) with O_2 administration. Mean differences between the first and third phase without and with administration of O_2 were −0.02 and 0.05, respectively. The limits of agreement for MCFR without administration of O_2 were between −0.36 and 0.31 (i.e. -0.02 ± 0.34) and between −0.13 and 0.23 (i.e. 0.05 ± 0.18) with O_2 administration.

4. Discussion

Our results demonstrated inhalation of 100% O_2 was significantly affected SpO_2 and MCFR (i.e. vascular resistance) in every phase and HR in third phase, and prolonged apnea did not significantly affect HR, SV and MCFR during breath-holding for three phases (42 s) regardless of 100% O_2 inhalation. To the best of our knowledge, the influence of prolonged apnea and inhalation of O_2 on pulmonary circulation during breath holding has not been addressed.

When considered the influence of inhaled O_2 before breath-holding and prolonged apnea on HR and SpO_2, mean HR for the third phase was significantly lower with administration of O_2 than without, and mean SpO_2 for each phase was significantly higher with administration of O_2 than without. Breath holding without O_2 administration significantly reduces SpO_2 for every phase. Previous study demonstrated that cardiac output under breath-holding had linear change in accordance with O_2 consumption due to an automatically mediated increase in HR [18]. Therefore, our results suggested that inhalation of 100% O_2 before breath holding could avoid decrease in O_2 consumption under prolonged apnea and significantly improve the increase in HR as compared with breath holding without O_2.

As for the influence of prolonged apnea and inhaled O_2 before breath-holding on SV and MCFR, prolonged apnea had no statistically significant influence on SV and MCFR. On the other hand, inhaled O_2 before breath-holding had a significant influence on MCFR at every phase. SV is defined as the difference between the right ventricular end-diastolic volume (EDV) and the end-systolic volume (ESV) unless valvular abnormalities exist. Changes in afterload affect the ability of the ventricle to eject blood and thereby alter SV. The effects of changes in EDV and ESV on SV are not independent, and an increase in ESV usually results in a compensatory increase in EDV [19]. Hypoxia induce pulmonary vasoconstriction and increase the pulmonary vascular resistance (i.e., an increase in the right ventricular afterload) [6,18]. The vasoconstriction recruits many previously unperfused pulmonary capillaries due to greatly increased pulmonary arterial pressure to maintain gas exchange for the lungs. This physiological reaction also increases the alveolar surface area available for gas diffusion, and improves the balance of ventilation and perfusion, in spite of reductions in SpO_2 and PaO_2 due to prolonged breath holding without administration of O_2 [18]. Therefore, our results suggested that apnea during three phases (44 s) induced by voluntary breath holding had no statistically significant influence on changes of SV and pulmonary vascular resistance, and inhaled O_2 before breath holding significantly reduced pulmonary vasoconstriction and decreased pulmonary vascular resistance during prolonged apnea.

Regarding the measuring agreement of hemodynamic indices during prolonged apnea without and with administration of O_2, the limits of agreement for the first and second phase during breath holding with administration of O_2 (0.9 ± 5.8 ml) were almost equal to those without administration of O_2 (1.2 ± 5.1 ml), while the corresponding limits of agreement for the first and third phase were similar (3.2 ± 8.7 and 3.7 ± 8.2 ml). In a typical heart, stroke volume is almost 70 ml [19]. Therefore, our results suggest that the measuring agreement of hemodynamic indices during prolonged breath holding without and with administration of O_2 were less than ±10% in short apnea (less than 28 s) and ±15% in prolonged apnea (equal to or more than 28 s and less than 42 s), and small enough for clinical purpose. In addition, when semi-quantitative or quantitative assessment of contrast-enhanced MR perfusion was performed by indicator dilution theory and central volume principle, influence of breath holding with or without inhalation of 100% O_2 on arterial input function (i.e. blood volume of main trunk of pulmonary artery) may be less than 15%, and small enough for clinical purpose. On the other hand, the limits of agreement of MCFR for the first and second phases (0.02 ± 0.09) and for the first and third phase (0.05 ± 0.18) were smaller with administration of O_2 than without (the limits of agreement between first and second phase: -0.13 ± 0.40, and between first and third phase: -0.02 ± 0.34). In addition, prolonged apnea with administration of oxygen doubled the value of limits of agreement. Therefore, although administration of O_2 allows us to acquire reproducible measurement of MCFR, prolonged apnea induce poor limits of agreement when compared with short breath holding.

Our study has certain limitations. First, number of subjects evaluated was limited in this study. Second, even though we used the parallel imaging technique in order to reduce scan time, the temporal resolution of velocity MRI and the number of scans during a single breath hold were less satisfactory than those obtained with "real-time" techniques such as echo-planar imaging [7], and may therefore not reflect the actual

physiological changes during breath holding with and without administration of O_2. Third, we only evaluated the effect of inhalation of O_2 on healthy volunteers, but not on patients with pulmonary diseases such as chronic obstructive lung disease, pulmonary thromboembolism and lung cancer. These patients may undergo various occurrences of hypoxia before and after breath holding, and would therefore show different effects of O_2 on pulmonary circulation parameters. Therefore, further examination of patients with pulmonary diseases seems to be warranted in order to determine the clinical utility of oxygen inhalation for measurement of pulmonary or systemic circulation parameters during breath holding. Fourth, we only evaluated SV and MCFR of the main trunk of the pulmonary artery during breath holding with and without administration of O_2, and did not utilize these parameters for a quantitative assessment of regional pulmonary perfusion parameters by using dynamic MR perfusion imaging, dynamic CT or PET. Until now, the modulation by inhalation of O_2 of regionally measured pulmonary perfusion parameters during breath holding has not been directly assessed. Therefore, further investigation in the near future for more accurate measurements of regional pulmonary perfusion parameters seems to be warranted. Such an investigation would combine velocity-MRI and quantitatively assessed dynamic MR imaging, dynamic CT and PET by using indicator dilution theory, central volume principle and the blood volume of the main trunk of the pulmonary artery as arterial input functions.

In conclusion, O_2 inhalation modulated maximal change in flow rate during ejection, and did not influence stroke volume during breath holding. Influence of O_2 inhalation should be considered for MR measurements of pulmonary hemodynamics during breath holding.

References

[1] Ohno Y, Hatabu H, Murase K, et al. Quantitative assessment of regional pulmonary perfusion in the entire lung using three-dimensional ultrafast dynamic contrast-enhanced magnetic resonance imaging: preliminary experience in 40 subjects. J Magn Reson Imaging 2004;20:353–65.

[2] Levin DL, Chen Q, Zhang M, et al. Evaluation of regional pulmonary perfusion using ultrafast magnetic resonance imaging. Magn Reson Med 2001;46:166–71.

[3] Meier P, Zierler KL. On the theory of the indicator-dilution method for measurement of blood flow and volume. J Appl Physiol 1954;6:731–44.

[4] Sakuma H, Kawada N, Kubo H, et al. Effect of breath holding on blood flow measurement using fast velocity encoded cine MRI. Magn Reson Med 2001;45:346–8.

[5] Ferrigno M, Hickey DD, Liner MH, et al. Cardiac performance in humans during breath holding. J Appl Physiol 1986;60:1871–7.

[6] Weinberger SE. Principles of pulmonary medicine. Philadelphia: Saunders; 2004.

[7] van den Hout RJ, Lamb HJ, van den Aardweg JG, et al. Real-time MR imaging of aortic flow: influence of breathing on left ventricular stroke volume in chronic obstructive pulmonary disease. Radiology 2003;229:513–9.

[8] Fink C, Ley S, Risse F, et al. Effect of inspiratory and expiratory breathhold on pulmonary perfusion: assessment by pulmonary perfusion magnetic resonance imaging. Invest Radiol 2005;40:72–9.

[9] Ley S, Fink C, Puderbach M, et al. MRI Measurement of the hemodynamics of the pulmonary and systemic arterial circulation: influence of breathing maneuvers. AJR Am J Roentgenol 2006;187:439–44.

[10] Mousseaux E, Tasu JP, Jolivet O, et al. Pulmonary arterial resistance: noninvasive measurement with indexes of pulmonary flow estimated at velocity-encoded MR imaging—preliminary experience. Radiology 1999;212:896–902.

[11] Wigstrom L, Ebbers T, Fyrenius A, et al. Particle trace visualization of intracardiac flow using time-resolved 3D phase contrast MRI. Magn Reson Med 1999;41:793–9.

[12] Lotz J, Meier C, Leppert A, et al. Cardiovascular flow measurement with phase-contrast MR imaging: basic facts and implementation. Radiographics 2002;22:651–71.

[13] Pruessmann KP, Weiger M, Scheidegger MB, et al. SENSE: sensitivity encoding for fast MRI. Magn Reson Med 1999;42:952–62.

[14] Thunberg P, Karlsson M, Wigstrom L. Accuracy and reproducibility in phase contrast imaging using SENSE. Magn Reson Med 2003;50:1061–8.

[15] Beerbaum P, Korperich H, Gieseke J, et al. Blood flow quantification in adults by phase-contrast MRI combined with SENSE—a validation study. J Cardiovasc Magn Reson 2005;7:361–9.

[16] Higgins CB, Roos Ad. Cardiovascular MRI and MRA. Philadelphia, Pa.: Lippincott Williams & Wilkins; 2003.

[17] Bland JM, Altman DG. Statistical methods for assessing agreement between two methods of clinical measurement. Lancet 1986;1:307–10.

[18] Levitzky MG. Pulmonary physiology. New York: McGraw-Hill Medical Publishing; 2003.

[19] Klabunde RE. Cardiovascular physiology concepts. Philadelphia: Lippincott Williams & Wilkins; 2005.

Postoperative Lung Function in Lung Cancer Patients: Comparative Analysis of Predictive Capability of MRI, CT, and SPECT

Yoshiharu Ohno[1]
Hisanobu Koyama[1]
Munenobu Nogami[1]
Daisuke Takenaka[1]
Sumiaki Matsumoto[1]
Masahiro Yoshimura[2]
Yoshikazu Kotani[3]
Kazuro Sugimura[1]

OBJECTIVE. The purpose of this study was to prospectively compare the utility of dynamic contrast-enhanced perfusion MRI in the prediction of postoperative lung function in patients with lung cancer with the utility of quantitative and qualitative assessment of CT and perfusion SPECT.

SUBJECTS AND METHODS. One hundred fifty lung cancer patients (87 men, 63 women) underwent dynamic perfusion MRI, MDCT, perfusion SPECT, and measurement of preoperative and postoperative forced expiratory volume in the first second of expiration (FEV_1) expressed as percentage of predicted value. Postoperative FEV_1 was predicted with dynamic perfusion MRI by semiquantitative assessment of the perfusion of whole lungs and resected segments of lungs, with quantitative assessment of functional lung volume on CT with commercially available software, with qualitative assessment of CT on the basis of the number of segments of total and resected lung, and with perfusion SPECT by assessment of uptake of microaggregated albumin particles in whole lungs and resected segments of lungs. Correlation and limits of agreement between actual and predicted postoperative FEV_1 values were statistically evaluated.

RESULTS. Actual postoperative FEV_1 had stronger correlation with postoperative FEV_1 predicted from perfusion MRI ($r = 0.87, p < 0.0001$) and quantitative CT ($r = 0.88, p < 0.0001$) than with postoperative FEV_1 predicted from qualitative CT ($r = 0.83, p < 0.0001$) and perfusion SPECT ($r = 0.83, p < 0.0001$). The limits of agreement between the actual postoperative FEV_1 and postoperative FEV_1 predicted from perfusion MRI (5.3% ± 11.8% [mean ± 2 SD]) were smaller than the values for postoperative FEV_1 predicted from qualitative CT (6.8% ± 14.4%) and perfusion SPECT (5.1% ± 14.0%) and was almost equal to the value for postoperative FEV_1 predicted from quantitative CT (5.0% ± 11.6%).

CONCLUSION. Dynamic perfusion MRI is more accurate in prediction of the postoperative lung function of patients with lung cancer than are qualitative CT and perfusion SPECT and may be at least as accurate as quantitative CT.

Keywords: cancer, lung cancer, lungs, MRI, perfusion, SPECT

DOI:10.2214/AJR.07.2084

Received December 5, 2006; accepted after revision February 28, 2007.

Presented at the 2006 annual meeting of the Radiological Society of North America, Chicago, Illinois.

Partially supported by the Knowledge Cluster Initiative of the Ministry of Education, Culture, Sports, Science and Technology of Japan; Philips Medical Systems; and Schering AG.

[1]Department of Radiology, Kobe University Graduate School of Medicine, 7-5-2 Kusunoki-cho, Chuo-ku, Kobe, Hyogo 650-0017, Japan. Address correspondence to Y. Ohno (yosirad@kobe-u.ac.jp).

[2]Division of Cardiovascular, Thoracic, and Pediatric Surgery, Kobe University Graduate School of Medicine, Kobe, Japan.

[3]Division of Cardiovascular and Respiratory Medicine, Department of Internal Medicine, Kobe University Graduate School of Medicine, Kobe, Japan.

AJR 2007; 189:400–408

0361–803X/07/1892–400

Lung cancer is the most common cause of cancer-related death among both men and women [1]. Despite advances in radiation therapy and chemotherapy, surgical resection remains the choice of treatment of patients with resectable non–small cell lung cancer. Nevertheless, it is estimated that only 20–25% of patients with non–small cell lung cancer undergo resection [2]. One reason for this low resection rate is that most patients with lung cancer have a history of cigarette smoking, which often engenders other conditions, such as chronic obstructive pulmonary disease and coronary artery disease, that can increase operative risk. Because clinicians are frequently asked to evaluate the risks and feasibility of lung resection for patients with multiple conditions, exercise testing and prediction of postoperative lung function have become increasingly important in the evaluation for lung resection [3, 4]. An algorithm for the functional assessment of candidates for lung resection has been proposed by Wyser et al. [5].

In current medical practice, ventilation–perfusion lung scintigraphy combined with spirometry is the most widely used radiologic examination when spirometric findings alone indicate pulmonary function may not be sufficient to tolerate resection [5]. The reported correlation coefficients of predicted and actual postoperative lung function measured with lung scintigraphy vary between 0.51 and 0.92 [5–11]; however, poor spatial resolution, especially troublesome for differentiating lobes and segments, is a major limi-

tation of this method. A few investigators [12, 13] have suggested perfusion SPECT may be more effective than perfusion scintigraphy for the prediction of postoperative lung function. Another approach to evaluating surgical risk for lung cancer patients is quantitative or qualitative evaluation based on lung attenuation or anatomic findings on CT [4, 5, 9–12]. Although the correlation between postoperative lung function predicted with quantitative assessment of CT and actual postoperative lung function has been excellent, qualitative assessment (i.e., simple calculation based on the number of segments of total and resected lung) is used by many clinicians.

It has been found that 3D dynamic contrast-enhanced perfusion MRI is useful for evaluation of regional pulmonary perfusion and assessment of physiologic and pathophysiologic conditions in healthy volunteers, animal models, and patients with pulmonary vascular disease [11, 14–19]. A few investigators compared the capability of this technique with that of perfusion scintigraphy in assessment of regional perfusion and prediction of outcome among lung cancer patients [11, 17]. The number of patients in those studies was limited, however, and the capability of perfusion MRI in prediction of postoperative lung function was not compared with the predictive capability of quantitative and qualitative assessment of CT (quantitative and qualitative CT). For our study, we planned prospective recruitment of a large cohort of patients with lung cancer. The purpose of the study was to prospectively determine the capability of dynamic contrast-enhanced perfusion MRI in prediction of postoperative lung function in direct comparison with the capability of quantitative and qualitative CT and perfusion SPECT.

Subjects and Methods

Subjects

The study cohort comprised 150 consecutively registered lung cancer patients (87 men, 63 women; age range, 43–85 years; mean, 66 years) considered candidates for lung resection. All of them underwent preoperative contrast-enhanced MDCT, dynamic perfusion MRI, perfusion SPECT, and measurement of preoperative and postoperative forced expiratory volume in the first second of expiration (FEV_1) expressed as percentage of predicted value. All preoperative radiologic examinations were performed in random order and less than 1 week before or after MRI (range, 1–6 days; mean, 3.2 days). Of the 150 patients, 87 had adenocarcinoma other than bronchioalveolar carcinoma, 47 had bronchioalveolar carcinoma, nine had squamous cell carcinoma, six had large cell carcinoma, and one had small cell carcinoma. The final diagnosis in all cases was confirmed with pathologic examination of resected specimens. Our institutional review board approved this study, and written informed consent was obtained from the subjects before they joined the study. Patient characteristics are summarized in Table 1.

TABLE 1: Patient Characteristics

Characteristic	Value
Age (y)	
Mean	66
Range	43–85
Sex (no.)	
Men	87
Women	63
Histologic subtype (no.)	
Bronchioalveolar carcinoma	47
Adenocarcinoma other than bronchioalveolar carcinoma	87
Squamous cell carcinoma	9
Large cell carcinoma	6
Small cell carcinoma	1
Operation (no.)	
Lobectomy	97
Bilobectomy	10
Pneumonectomy	5
Segmentectomy	38
Predicted preoperative FEV_1 (percentage of predicted value)	
Mean ± SD	85.1 ± 15.0
Range	45.0 – 120.0
Actual postoperative FEV_1 (percentage of predicted value)	
Mean ± SD	74.0 ± 11.9
Range	49.0 – 99.8

Dynamic Contrast-Enhanced Perfusion MRI

All MRI studies were performed on a 1.5-T MRI unit (Gyroscan Intera, Philips Medical Systems) with a phased-array coil. Dynamic perfusion MRI (TR/TE, 2.7/0.6; flip angle, 40°; matrix size, 128 × 96; reconstructed matrix size, 256 × 192; rectangular field of view, 450–530 × 315–371 mm) were acquired with a 3D radiofrequency spoiled gradient-echo sequence. A 3D slab thickness of 100 mm was used with 10 partitions and an overlapping slice in the coronal plane in a left-to-right phase-encoded direction. The result was an effective partition thickness of 10 mm and five-step real-phase encoding in the slice direction. The temporal resolution was 1.0 second for each 3D data set. All patients received 3–5 mL of gadopentetate dimeglumine (Magnevist, Schering) in a bolus administered through an antecubital vein with an automatic infusion system (Sonic shot, Nemoto) at a rate of 3–5 mL/s followed by 20 mL of saline solution at the same rate. The basic theory and application of dynamic perfusion MRI have been documented in the past literature [11, 16, 19]. After careful instruction, patients practiced the breath-hold technique to reproduce precisely the same degree of inspiration for each MR image series. In each acquisition, 25 images were obtained during a 25-second breath-hold at end inspiration. All 150 dynamic contrast-enhanced perfusion MRI examinations were completed successfully without adverse effects.

Image and Data Analysis of Dynamic Contrast-Enhanced Perfusion MRI

Signal intensity–time course curves after administration of gadopentetate dimeglumine were generated by measurement of the signal intensity in regions of interest (ROIs) delineated with our proprietary software in the right upper, right middle, right lower, left upper, left middle, and left lower lung fields in every slice of every subject (60 ROIs per patient). Large vessels and pulmonary arteries were excluded from the ROIs. From each ROI, data were transferred to a PC (FMV-900, Fujitsu) and were analyzed with Excel 2003 software (Microsoft) by a chest radiologist with 13 years of experience.

For extraction of quantitative indexes, the signal intensity–time course curves were fitted to a gamma variate function with the following equation [11, 16]:

$$S_{(t)} = S_{peak}\left(\frac{e}{\alpha\beta}\right)^{\alpha}(t-T_a)^{\alpha}e^{[-(t-T_a)/\beta]} + S_0$$

where t is the time, $S_{(t)}$ is the measured signal intensity as a function of time, S_0 and S_{peak} are the baseline and peak signal intensities, T_a is the arrival time of the contrast bolus, and α and β are fitting parameters of the gamma variate function. Because of the small dose of injected contrast agent used, it was assumed that a linear relation exists between first-pass MRI signal intensity and contrast medium concentration in the ROI.

From the gamma variate function, the following equation [11, 16] was used to calculate the apparent mean transit time as the first moment on the MRI signal intensity–time course curve:

$$\text{Mean transit time} = \frac{\int t \times (S_{(t)} - S_0)\,dt}{\int (S_{(t)} - S_0)\,dt}$$

Regional pulmonary blood volume was calculated directly from the area of the MRI signal inten-

sity–time course curve for a given ROI. According to the central volume principle, regional blood flow in each ROI (Q_{ROI}) was determined by dividing pulmonary blood volume by mean transit time [11, 16, 19]. The Q_{ROI} value was then normalized to the integrated arterial input function from the main trunk of the pulmonary artery [11, 16]. The approximate time for an ROI measurement was 1 minute.

To determine regional perfusion in a lung field on dynamic contrast-enhanced perfusion MRI for prediction of postoperative lung function, blood flow in an ROI evaluated with dynamic perfusion MRI (Q_{MRI}), expressed as a percentage, was calculated as follows:

$$Q_{MRI} = \frac{\sum_{n=1}^{10} Q_{ROI(n)}}{\sum_{n=1}^{10}(Q_{RUL(n)} + Q_{RML(n)} + Q_{RLL(n)} + Q_{LUL(n)} + Q_{LML(n)} + Q_{LLL(n)})} \times 100$$

where n is the slice number, $Q_{ROI(n)}$ is the blood flow of the ROI, $Q_{RUL(n)}$ is the blood flow of the right upper lung field, $Q_{RML(n)}$ is the blood flow of the right middle lung field, $Q_{RLL(n)}$ is the blood flow of the right lower lung field, $Q_{LUL(n)}$ is the blood flow of the left upper lung field, $Q_{LML(n)}$ is the blood flow of left middle lung field, and $Q_{LLL(n)}$ is the blood flow of the left lower lung field, all on slice n.

To evaluate capability in prediction of postoperative lung function, postoperative FEV_1 predicted with dynamic perfusion MRI was calculated as follows:

$$\text{Postoperative } FEV_1 \text{ from perfusion MRI} = FEV_1 \times \left(1 - \frac{Q_{MRI} \text{ of resected lung or lobe}}{100}\right)$$

The details of calculation of regional blood flow and postoperative FEV_1 predicted from perfusion MRI have been described in the literature [11].

CT Examination

All CT examinations were performed with an MDCT scanner (Somatom Plus 4 Volume Zoom, Siemens Medical Solutions). The scans were obtained from the lung apex to the diaphragm (collimation, 4 × 1 mm; pitch, 6:1; field of view, 300–350 mm; matrix size, 512 × 512; 330 mA at 140 kV) and reconstructed as 5-mm-thick slices. Before CT, patients practiced breathing to produce full and consistent inspiration. CT was performed during a breath-hold at the end of full inspiration. Contrast medium (iopamidol, Iopamiron 300, Schering Japan) was administered IV with a power injector (Auto Enhance-50, Nemoto) at 2–3 mL/s through an antecubital vein with an empiric scan delay of 20 seconds to delineate the boundaries between tumor and mediastinal structures.

Image and Data Analysis of CT

Quantitative prediction of postoperative lung function—For quantitative prediction of postoperative lung function from functional lung volume, we used an assessment method described in the literature [10, 11]. After applications of dual thresholds of –500 and –910 H, total functional lung volume and regional functional lung volume of the lung or lobe to be resected were calculated by multiplying the area of each functionally relevant lung tissue by the slice thickness. The area of associated emphysema was excluded by the lower threshold value (–910 H). Areas of tumor-related air space loss, such as the tumor itself and postobstructive atelectasis, and areas of air space loss not related to the tumor, such as fibrosis and atelectasis due to previous tuberculosis, were satisfactorily excluded during visual inspection of the functional lung volume map. A chest radiologist with 15 years of experience used commercially available software (Pulmo, Siemens Medical Solutions) to perform all quantitative assessments of functional lung volume.

Predicted postoperative FEV_1 evaluated by quantitative assessment of CT scans was calculated from total functional lung volume and regional functional lung volume with the following equation [10, 11, 20]:

$$\text{Postoperative } FEV_1 \text{ from quantitative CT} = \text{Preoperative } FEV_1 \times \left(1 - \frac{\text{Regional funtional volume of resected lung or lobe}}{\text{Total functional lung volume}}\right)$$

The regional functional lung volume of resected lung or lobe was determined for each slice as the sum of regional functional lung volumes calculated from ROIs placed on the resected lobe or lung.

Qualitative prediction of postoperative lung function—For qualitative prediction of postoperative lung function, postoperative FEV_1 was obtained from preoperative pulmonary function test data and information on the number of bronchopulmonary segments removed obtained according to a method used in many surgical institutions [3, 20–23]. For determination of the number of bronchopulmonary segments removed, all studies were interpreted by a chest radiologist with 7 years of experience and by a pulmonary surgeon with 24 years of experience; final assessments were made in consensus. The postoperative FEV_1 predicted with qualitative assessment of CT scans was estimated with the following formula [3, 20–23]:

$$\text{Postoperative } FEV_1 \text{ qualitative CT} = \text{Postoperative } FEV_1 \times (1 - S \times 0.0526)$$

where S is the number of bronchopulmonary segments removed by lung resection. Each segment is considered to represent 1/19 of lung function (1/19 = 0.0526). The lower lobes were considered to have five pulmonary segments each, the upper lobe of the right lung to have three segments, the middle lobe of the right lung to have two segments, and the upper lobe of the left lung to have four segments [3, 20–23].

Perfusion SPECT Examination

All perfusion SPECT data were obtained with a SPECT system (e-CAM, Siemens Medical Solutions) equipped with a medium-energy all-purpose collimator and with the subject in the supine position. All perfusion SPECT examinations were performed without respiratory gating and with IV administration of 185 MBq of ^{99m}Tc–microaggregated albumin. Images were acquired in 60 projections over 360° by the step-and-shoot method. The integration time per image was 20 seconds, and the matrix size was 64 × 64. A total of 38–49 6.4-mm-thick transaxial sections covering both whole lungs were reconstructed with a Butterworth filter (order, 8; cutoff frequency, 0.34 cycle/cm) and a ramp back-projection filter. The energy window of ^{99m}Tc was 140 keV ± 10%. The lung contour was drawn at a threshold of 20% of the maximum radioactivity of the lung.

Image and Data Analysis of Perfusion SPECT

For prediction of postoperative lung function with the aid of SPECT with ^{99m}Tc–microaggregated albumin, ROIs were placed over the lobe that